Green Chemistry

PAPER

View Article Online
View Journal | View Issue

Cite this: *Green Chem.*, 2025, **27**, 9696

Regulation of lithium ion transport dynamics *via* a carbonized-polymer-dot-modified substrate to achieve 2 mV ultralow voltage hysteresis†

Jiayu Zhang,‡[a] Yanfei Li,‡[b] Yihan Song,[a] Guoduo Yang,[a] Zhuo Wang,[a] Xinyao Huang[a] and Haizhu Sun *[a]

The practical implementation of lithium metal remains challenging because of unregulated Li dendrite growth, which results in safety hazards and poor cycling performance. Herein, a stable three-dimensional (3D) hybrid architecture with low voltage hysteresis is fabricated by modifying N,O-codoped carbonized-polymer-dots (CPDs) on a carbon-based substrate (CPDs-GCC). CPDs provide an abundance of lithiophilic nitrogen-containing functional groups and carbonyl groups, which can direct the homogeneous deposition of lithium and reduce the growth of Li dendrites. Moreover, the CPD-based lithiophilic anode reduces the migration energy barrier and activation energy of Li^+, enhances the exchange current density, and effectively enhances the ion transport kinetics and ion reaction kinetics at the electrode–electrolyte interface. As a result, the half cells with a capacity of 3 mAh cm^{-2} allow an ultralow voltage hysteresis of ~2 mV over 4800 h at 2 mA cm^{-2}. The full cell with a $LiFePO_4$ cathode demonstrates outstanding cycling stability with a capacity retention of 95% after 3000 cycles at 0.2 A g^{-1}. This study examines the factors influencing voltage hysteresis, explores its impact on battery performance, and proposes a simple method to mitigate it. This lays the foundation for the development of high-performance batteries.

Received 25th April 2025,
Accepted 11th July 2025

DOI: 10.1039/d5gc02081f

rsc.li/greenchem

Green foundation

1. Compared to metal-based materials, carbon-based alternatives provide sustainable advantages through abundant sources and avoid mining/smelting processes, significantly reducing production energy and non-renewable resource dependence.
2. This work demonstrates an ultra-low hysteresis Li anode *via* carbonized polymer dots (CPDs) on carbon current collectors. Different from metal-based systems, CPDs feature simple, green synthesis without organic solvents or toxic heavy metals (Ni, Co), preventing environmental contamination.
3. The use of biomass small molecules as precursors for the synthesis of CPDs can further diversify the raw material sources of carbon and enhance the potential for waste utilization. However, challenges remain in exploring the relationship between the structure of CPDs and the improvement of battery performance to select appropriate biomass small molecules.

1. Introduction

Due to the very low reduction potential (−3.04 V *vs.* SHE) and high theoretical capacity (3860 mAh g^{-1}), lithium metal batteries (LMBs) are considered as some of the most promising anodes to provide energy storage and fulfill future demands.[1–7] However, uncontrollably growing dendrites, limitless volume expansion, nonuniform charge allocation formed on the electrode/electrolyte and cracking of the solid electrolyte interphase (SEI) have prevented the development of viable rechargeable batteries with Li metal anodes.[8–12] Considerable work has been done to solve these problems, including the creation of a three-dimensional (3D) network, the fabrication of artificial coating layers, the regulation of electrolyte components, *etc.*[13–18]

To address these issues, controlling Li nucleation behavior is important, which is known to be significantly impacted by matrix surface properties.[19] Consequently, the modification of 3D current collectors has consistently been a key focus of investigation in this field. A successful modification will lead to a high coulombic efficiency (CE) and low voltage hysteresis.

[a]*College of Chemistry, National & Local United Engineering Laboratory for Power Batteries, Northeast Normal University, No. 5268, Renmin Street, Changchun, 130024, P. R. China. E-mail: sunhz335@nenu.edu.cn*
[b]*State Key Laboratory of Organic Electronics and Information Displays & Institute of Advanced Materials (IAM), School of Chemistry and Life Sciences, Nanjing University of Posts & Telecommunications (NJUPT), Nanjing 210023, P. R. China*

†Electronic supplementary information (ESI) available. See DOI: https://doi.org/10.1039/d5gc02081f

‡These authors contributed equally to this work.

A high CE is typically indicative of enhanced anode utilization, while low voltage hysteresis is commonly correlated with improved cycling stability. For instance, Yang and co-workers produced a 3D current collector on copper foam that induced consistent and stable Li deposition by anchoring graphene, which maintained a CE of 97.4% at 2 mA cm^{-2} after 150 cycles and afforded an area capacity of 6 mAh cm^{-2} at 6 mA cm^{-2} in symmetric cells.[13] Liu and co-workers reported a gradient-pore-size carbon skeleton as the lithium metal anode. The anode exhibited a modest and steady voltage polarization of ~15 mV over 1000 h.[20]

Although substantial progress has been made in enhancing CE, research on voltage hysteresis remains limited. On the one hand, the concept of voltage hysteresis remains poorly defined, with many studies only superficially addressing it without elucidating the underlying mechanisms, which leads to voltage polarization being limited to approximately 10–20 mV in most materials. On the other hand, the relationship between voltage hysteresis and cycling stability is not well elucidated, hindering the analysis of abrupt changes in voltage hysteresis during long-term cycling. Therefore, investigating the factors influencing voltage hysteresis and their relationship with cycling stability is of great significance.

Herein, a novel strategy is developed to modify N,O-codoped carbonized polymer dots (CPDs) on the surface of cotton cloth covered with reduced graphene oxide (rGO), namely, CPDs-GCC, which can be applied as a 3D stable lithium anode substrate to achieve ultralow voltage hysteresis and enhance the cycling stability. The material surface is rich in functional groups, making it have tremendous potential to induce homogeneous nucleation and deposition of lithium metal.[21–25] The electrode fabricated based on CPDs-GCC reduces the migration energy barrier and activation energy of Li^+, increases the exchange current density, and effectively enhances the ion transport kinetics and ion reaction kinetics at the electrode–electrolyte interface. The experimental results show that the N,O-codoped CPDs significantly improve the lithiophilicity and enable stable operation for over 4800 h at 2 mA cm^{-2}, with a voltage hysteresis as low as 2 mV in symmetric cells. Specifically, the full cell with a $LiFePO_4$ cathode can maintain 95% capacity (139 mAh g^{-1}) after 3000 cycles at 0.2 A g^{-1}. Even under substantial deformation, the assembled flexible lithium metal batteries (FLMBs) retain outstanding flexibility and stability.

2. Results and discussion

2.1. Structure and morphology of CPDs-GCC

Scheme 1 displays the synthetic procedure of the CPDs-GCC. Firstly, non-woven cotton cloth (CC) is chosen as the substrate material for the Li metal anode, which is cheap and exhibits flexible properties. The network structure of cotton cloth (CC) exhibits a large specific surface area due to its fibrous skeleton structure, which lowers the effective current density. After the addition of graphene oxide (GO) and annealing, reduced graphene oxide (rGO) is evenly distributed on the surface of each CC fiber, which improves the conductivity of the substrate. Finally, the uniform distribution of CPDs in rGO-CC (CPDs-GCC) brings the substrate with abundant nitrogen-containing functional groups and carbonyl groups, which will guide uniform Li deposition with small voltage polarization.

Carbonized polymer dots were prepared based on the classical hydrothermal synthesis method.[26] The morphology of the

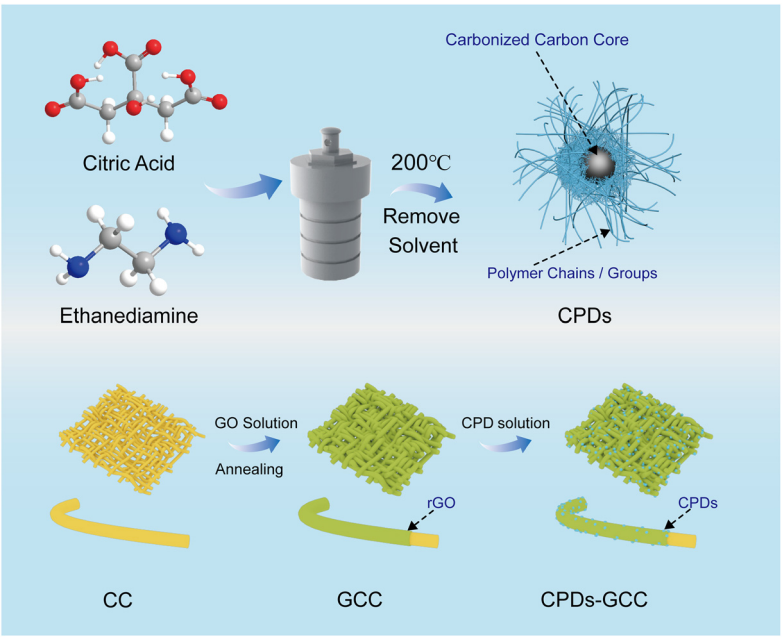

Scheme 1 Schematic illustration of the preparation of CPDs and the CPD-GCC substrate.

synthesized CPDs is studied by transmission electron microscopy (TEM). Fig. S1a† shows the TEM images of CPDs with diameters in the range of 1.3–3.4 nm. The HRTEM image of CPDs in Fig. S1b† shows that the parallel plane spacing is 0.21 nm. A broad peak at 21° observed in X-ray diffraction (XRD) patterns indicates the low crystallinity of CPDs (Fig. S2†). As shown in Fig. S3,† the Fourier transform infrared (FT-IR) spectrum of the CPDs exhibits the stretching vibrations of –OH at 3430 cm^{-1}, –NH at 2923 cm^{-1} and C–H at 2850 cm^{-1}, the vibrational absorption band of C=O at 1635 cm^{-1}, the bending vibrations of N–H at 1570 cm^{-1}, and the asymmetric bending vibrations of –C–NH–C– at 1126 cm^{-1}. Through the survey X-ray photoelectron spectroscopy (XPS) spectrum shown in Fig. S4a,† abundant C, O, and N elements on the surface of the CPDs are confirmed to be present. According to the atom content listed in Table S1,† the contents of elements C, O and N are 71.04%, 16.83% and 12.13%, respectively. In Fig. S4b,† the peaks of C–C (284.8 eV), C–O (286.0 eV), C–N (287.7 eV) and O–C=O (288.9 eV) are observed in the high-resolution C 1s of CPDs. In high-resolution N 1s, the peaks of $–NH_2$ (398.9 eV), pyrrolic N (400.3 eV) and graphite N (401.9 eV) are observed (Fig. S4c†). As shown in Fig. S4d,† O 1s analysis reveals three different types of oxygen atoms: C–O (531.0 eV), O–H (531.9 eV) and C=O (533.3 eV). These results confirm the presence of abundant functional groups, especially the carbonyl groups and N-containing groups, on the surface of CPDs.

A smooth surface of CC is clearly visible from the scanning electron microscopy (SEM) image, as illustrated in Fig. 1a. It is shown that there are some interval gaps and pores that exist on the CC (Fig. S5†). After GO is coated on CC through an easy wetting operation (denoted as GO-CC), the color of CC changes from white to dark brown, confirming the successful synthesis of GO-CC (Fig. 1i). Reduced graphene oxide was coated on cotton cloth by treating GO-CC in ammonia after annealing, where GO was converted into rGO and CC was partially graphitized (denoted as GCC). 700 °C is the optimized reaction temperature for the annealing treatment (Fig. S6†). As compared with CC, the annealed GCC has typical graphene folds with a rough surface as shown in Fig. 1b, in which rGO is uniformly distributed. The SEM elemental mapping image of GCC is shown in Fig. S7,† showing that C and O elements are homogeneously distributed in GCC.

CPDs-GCC was synthesized through simple solution immersion. No distinct morphology change is observed on the SEM images of GCC and CPDs-GCC (Fig. 1c), and the CPD-GCC substrate maintains the 3D structure of CC and GCC (Fig. S8 and S9†). Additionally, each treatment step leaves the cloth flexible, making it possible for the substrate to be folded and coiled into various forms without compromising its structural strength (Fig. 1i). As shown in Fig. 1d, CPDs are obviously identified in the TEM image, confirming their uniform distribution. The consistent distribution of C, O, and N elements in CPDs-GCC is evident in Fig. 1e–h. Compared with the mapping of GCC (Fig. S7†), the presence of N elements in CPDs-GCC is attributed to the CPDs.

Confocal laser scanning microscopy (CLSM) is used to clearly demonstrate the existence of CPDs due to the common fluorescent nature of carbon dots (Fig. S10†). After deposition, there is an obvious fluorescent signal on the fiber of CPDs-

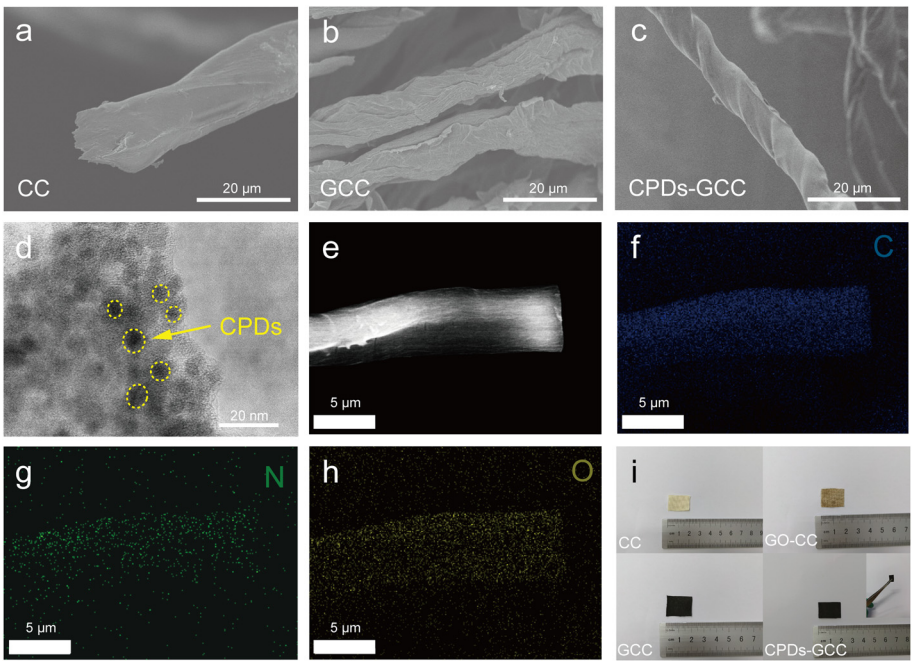

Fig. 1 (a–c) SEM images of CC, GCC and CPDs-GCC. (d) TEM image of CPDs-GCC. (e–h) SEM elemental mapping images of CPDs-GCC. (i) Digital photographs.

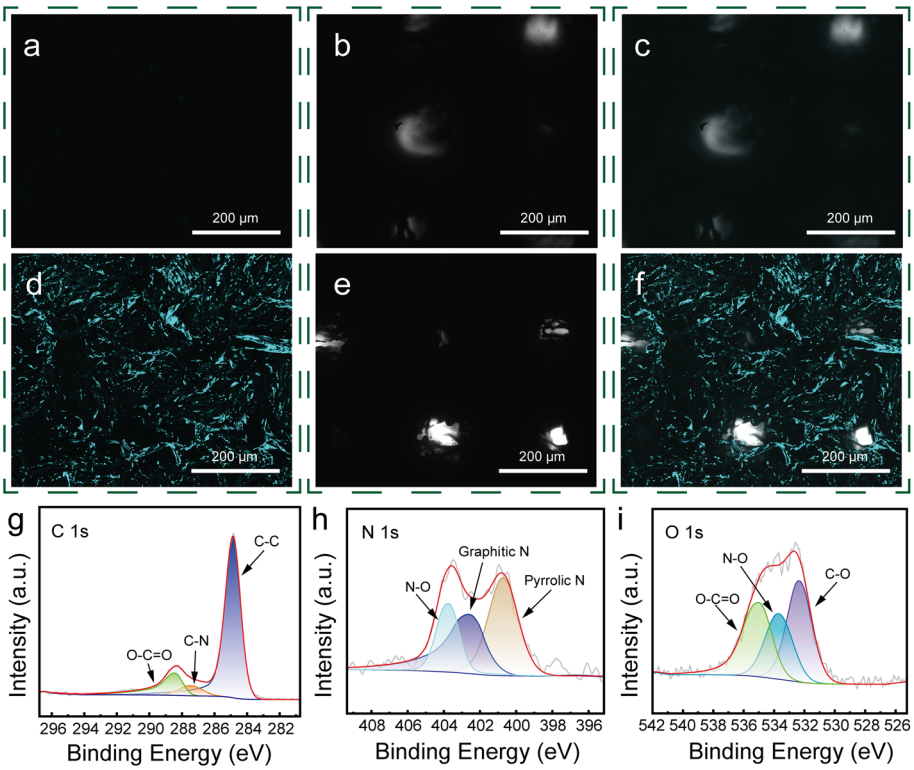

Fig. 2 Confocal luminescence images of GCC (a–c) and CPDs-GCC (d–f), respectively, in bright field (a and d), dark field (b and e) and compound field (c and f). High-resolution XPS spectra of (g) C 1s, (h) N 1s and (i) O 1s of CPDs-GCC.

GCC, which clearly shows a homogeneous distribution in Fig. 2d–f. No fluorescent signal is found on GCC as expected in Fig. 2a–c. The above result suggests that these CPDs are tightly grown on the surface of GCC.

In connection with XPS, the surface information of CPDs-GCC is also ascertained. The major elements on the surface of CPDs-GCC are C, N and O (Fig. S11†). Compared to GCC (Fig. S12†), the CPD-GCC surface has nitrogen that is not present on GCC, and the percentage of oxygen increases from 8.93 to 32.4 at% (Tables S2 and S3†). The increase of N and O atoms originates from the CPDs attached to the surface of CPDs-GCC. The C–C, C–N, and O–C=O peaks in the C 1s spectrum are located at 284.86 eV, 287.47 eV, and 288.44 eV, respectively (Fig. 2g). The N 1s signals are composed of three peaks at 400.72 eV, 402.58 eV and 403.72 eV, which correspond to the pyrrolic N, graphitic N and N–O bonds, respectively (Fig. 2h). As shown in Fig. 2i, O 1s signals are deconvoluted into three peaks at 532.33 eV, 533.69 eV and 534.99 eV, which correspond to the C–O, N–O and O–C=O, respectively. An obvious change in XPS spectra confirms that CPDs alter the chemical environment of the material by introducing N-containing groups and O-containing groups on the surface.

2.2. Modulation of lithium uniform deposition by CPDs-GCC

The half cells with GCC or CPDs-GCC as substrates and Li foil as the counter electrode were fabricated in order to study the material as an anode for the Li metal deposition process. The voltage gradually enters a smooth plateau below 0 V (*versus* Li^+/Li) after discharging to 2.5 mAh cm^{-2} in CPDs-GCC, demonstrating deliberate Li deposition on the anode (Fig. S13†). Spherical metallic Li particles gradually appear while plating 5 mAh cm^{-2} of Li in GCC (Fig. S14a†). When plating at 7 mAh cm^{-2}, Li particles gradually grow into a mossy morphology (Fig. S14b†). With a 9 mAh cm^{-2} composite anode, Li dendrites are clearly visible growing on the GCC anode surface in Fig. S14c.† As a comparison, the SEM images of CPDs-GCC demonstrate that Li is dispersed across the whole host and is uniformly plated on the carbon-based framework (Fig. S14d†). With further plating, the surface morphology of the anode still remains smooth without dendritic Li (Fig. S14e and f†).

To investigate the mechanism behind the dendrite-free lithium deposition behavior on CPDs-GCC, we calculated the interaction energies between Li^+ and the most abundant functional groups on CPDs, namely pyrrolic N and carboxyl (–COOH) groups. Density functional theory (DFT) calculations revealed that the binding energy between Li and the C=O in –COOH is −2.38 eV, while that between Li and pyrrolic N is −2.76 eV, both significantly higher than the binding energy between Li and the C–C bonds in GCC (Fig. 3a and b).[27] These higher binding energies indicate that the abundant functional groups on CPDs serve as active adsorption sites for Li, thereby reducing the nucleation energy barrier for Li deposition. To experimentally verify the interaction between Li and the func-

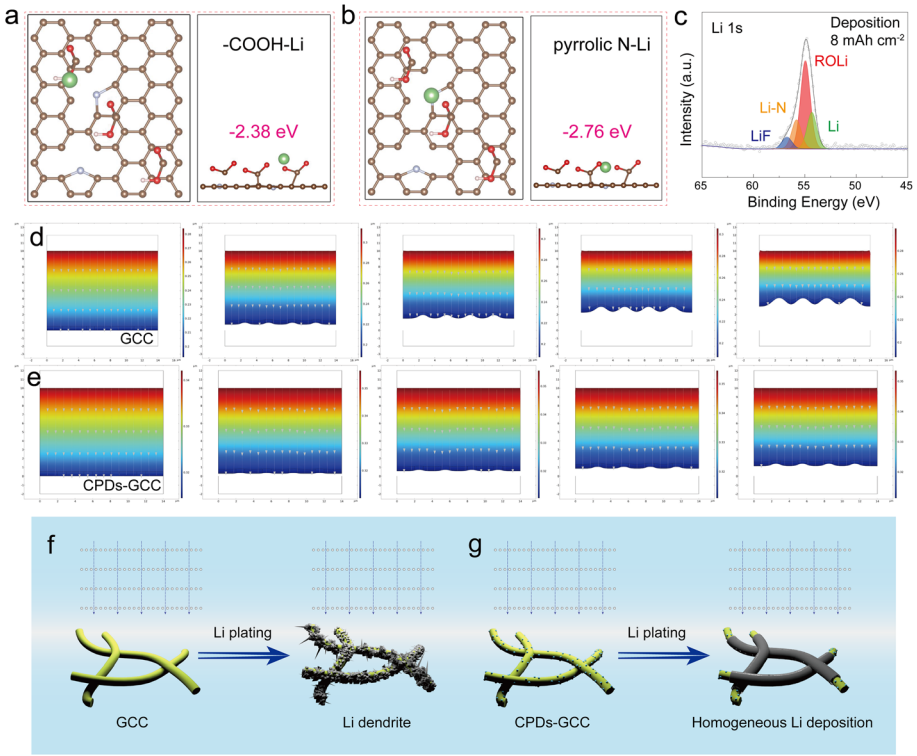

Fig. 3 Schematics of the model for bonding energy calculation between Li and different functional group atoms, and its corresponding Li adsorption energies. (a) −COOH−Li and (b) pyrrolic N−Li. (c) XPS spectrum of Li 1s for the CPD-GCC anode after Li deposition. Simulated ion concentration distributions during the process of Li deposition on different anodes: (d) GCC and (e) CPD-GCC anodes. (f and g) Illustration of Li plating on the GCC and CPD-GCC anodes.

tional groups, XPS was performed on the CPD-GCC anode after depositing 8 mAh cm^{-2} of Li (Fig. 3c). Deconvolution of the Li 1s spectrum yielded four peaks: the peak at 54.3 eV corresponds to metallic Li, while the peaks at 55.0 eV and 55.8 eV are attributed to O–Li bonds (from carbonyl groups) and Li–N bonds (from pyrrolic N), respectively. The peak at 56.8 eV corresponds to Li–F species, originating from the LiTFSI in the electrolyte. These results confirm the chemical interactions between Li and the pyrrolic N and carboxyl groups on CPDs, consistent with the DFT predictions. Moreover, similar results were observed after 20 cycles, further confirming the stability of these lithiophilic functional groups (Fig. S15†).

To further elucidate the role of functional groups in Li deposition behavior, COMSOL simulations were performed to model the Li^+ concentration field near the electrode surface. Due to the poor lithiophilicity of GCC, a steep Li^+ concentration gradient developed at its surface, leading to uneven deposition and the formation of dendritic protrusions over time (Fig. 3d). In contrast, the incorporation of CPDs significantly mitigated the concentration gradient at the CPD-GCC surface, effectively suppressing dendrite growth and promoting uniform Li^+ deposition (Fig. 3e). This indicates that the addition of a CPD functional group can effectively inhibit the development and expansion of Li dendrites (Fig. 3f and g).

The deposition morphology on the bare Cu electrode and CPDs-GCC electrode during Li plating was also tested in open cells (Fig. S16†). After 5 min of plating, dendrites nucleate on the surface of Cu foil. The size of the dendrites grows as the plating progresses, while the surface morphology of CPDs-GCC does not change noticeably in the whole process of plating. Therefore, the CPD-GCC current collector mitigates the deadly problem of dendritic development.

2.3. Electrochemical properties of CPD-GCC based electrodes

To investigate the electrochemical performance of the CPD-GCC substrate, the CE test was carried out. Initially, CPDs-GCC was cycled five cycles for the formation of a solid electrolyte interphase (SEI). The almost coincident curves prove that an SEI has been stably formed (Fig. S17†). With an areal capacity of 1 mAh cm^{-2} and a current density of 2 mA cm^{-2}, CPDs-GCC exhibits a rather high and stable CE of 99% over 180 cycles (Fig. 4a). The GCC, in comparison, exhibits a quick deterioration to 77% in CE after just 110 cycles. The CE of the CC vacillates up and down from less than 20 cycles and reaches a full stop at 30 cycles. Impressively, while plating Li on the CPDs-GCC with greater areal capacities of 4 mAh cm^{-2} and 8 mAh cm^{-2}, respectively, it is still able to maintain a high and consistent CE of 95% at 140 cycles and 98% at 120 cycles (Fig. S18†).

The amount of CPDs added has also been explored. Various quantities of CPDs were dispersed to generate an aqueous solution (40 mg, 70 mg and 100 mg of CPDs were distributed

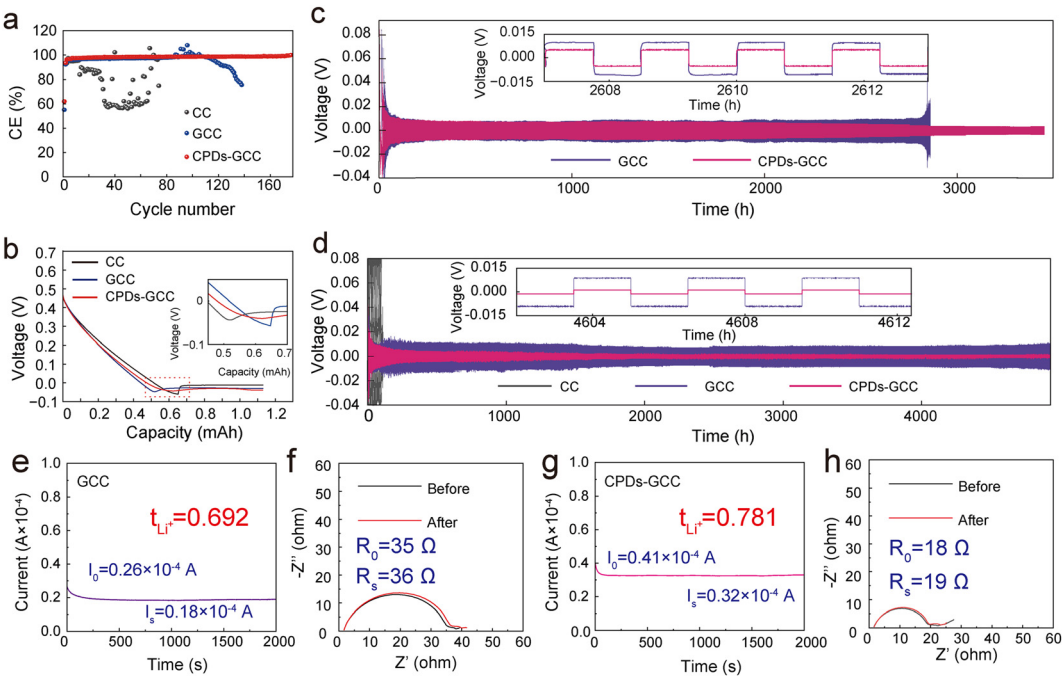

Fig. 4 (a) CE of Li plating/stripping on/from the CC, GCC and CPDs-GCC at current densities of 2 mA cm^{-2} with an areal capacity of 1 mAh cm^{-2}. (b) The initial voltage profiles of CC, GCC and CPDs-GCC. (c) Voltage profiles in symmetric cells of CC//Li, GCC//Li and CPDs-GCC//Li in 1 mAh cm^{-2} at 2 mA cm^{-2} and (d) in 3 mAh cm^{-2} at 2 mA cm^{-2}. Inset: magnified voltage profiles. The Li$^+$ transference number test for (e) GCC and (g) CPDs-GCC. The EIS test for (f) GCC and (h) CPDs-GCC.

in 10 mL of deionized water), and GCC samples were submerged in the three different aqueous solutions, respectively, denoted as 40 mg CPDs-GCC, 70 mg CPDs-GCC and 100 mg CPDs-GCC. The results reveal that 70 mg CPD-GCC cycled stably for more than 200 cycles with a CE of more than 97%, but 40 mg CPDs-GCC and 100 mg CPDs-GCC suffer a catastrophic short circuit after 80 and 40 cycles, respectively (Fig. S19†).

Furthermore, to clarify Li deposition behavior, a thorough investigation of voltage polarization was conducted. Fig. 4b shows a comparison of the Li plating voltage profiles on the CC, GCC, and CPDs-GCC. There is a noticeable voltage decrease when Li deposits on the material, and then a level voltage plateau follows. The Li metal nucleation overpotential is defined as the difference between the bottom of the voltage drop and the flat part of its plateau, which is mostly determined by the properties of the substrate. The nucleation potential of the CC was about 48 mV, which is much higher than the nucleation potentials of the GCC (21 mV) and CPDs-GCC (13 mV). The minimal nucleation overpotential of the CPDs-GCC is in accordance with uniform Li nucleation.

Galvanostatic cycling performance was used to evaluate the voltage hysteresis and long-term cycling stability of the anode (with Li foil as the counter electrode). The cycling stability of CPDs-GCC is maintained up to 3400 h at 2 mA cm^{-2} and 1 mAh cm^{-2}, while a short circuit occurs in GCC symmetric cells after 2850 h (Fig. 4c). For a certain current density of 2 mA cm^{-2} at 3 mAh cm^{-2}, these three types of symmetric coin cells were operated (Fig. 4d). Markedly, the CPD-GCC cell displays a stable voltage profile and an incredibly long lifespan of 4800 h, which is either better than or equal to the results that have been previously reported (Table S4†). In contrast, the GCC cell shows a fluctuant voltage profile with substantially greater voltage polarization, and CC exhibits a short circuit after 100 h. Moreover, CPDs-GCC exhibits a higher Li$^+$ transference number. Compared with that of GCC (0.692, Fig. 4e), the Li$^+$ transference number of CPDs-GCC reaches as high as 0.781 (Fig. 4g). Fig. 4f and h show the electrochemical impedance spectra of the GCC cell and the CPDs-GCC cell before and after the it test. Notably, the half-cell assembled with the CPD-GCC anode demonstrates remarkably low voltage hysteresis and rapid ion kinetics during galvanostatic charge–discharge cycling. This intriguing performance prompted us to investigate the underlying mechanisms in detail.

2.4. Mechanistic investigation

In symmetric cells, voltage hysteresis is defined as the difference between the steady voltage and 0 V during constant current charge–discharge cycles. During the charging process, Li$^+$ ions from the electrolyte migrate to the surface of the anode, where they undergo reduction by accepting electrons and are subsequently plated as lithium metal onto the electrode. Within a specific capacity range, the charge transfer capability at the lithium metal–electrolyte interface is adequate to sustain the deposition and stripping of lithium. However, as the deposition rate and capacity increase, an increasing

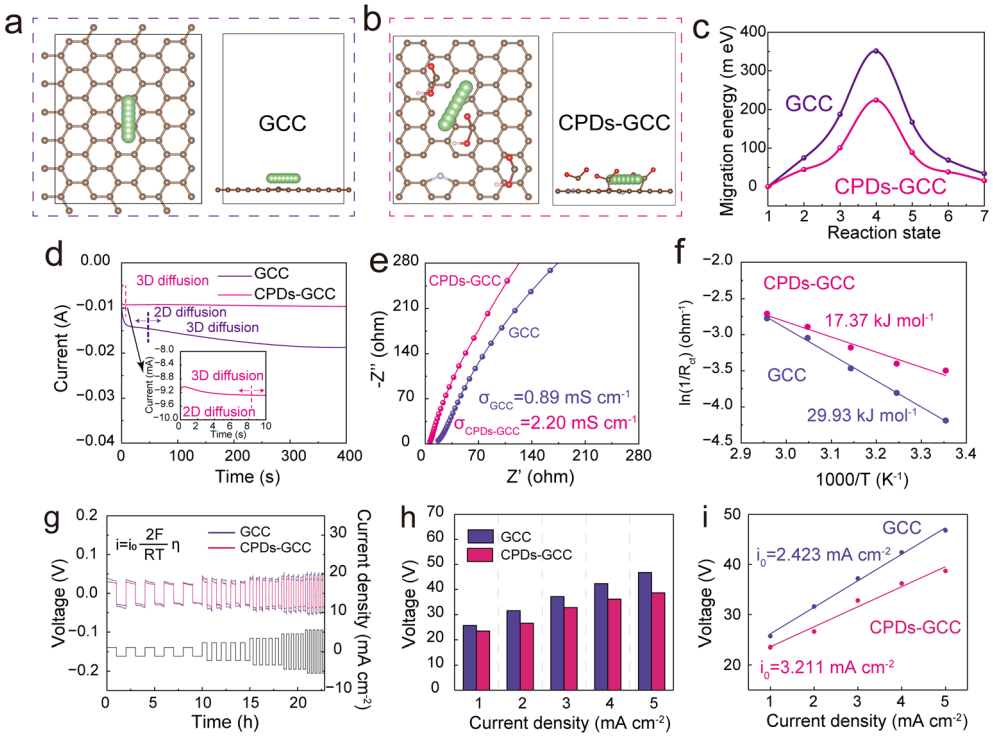

Fig. 5 Diffusion pathways of Li^+ on the surface of (a) GCC and (b) CPD-GCC anodes. (c) Corresponding migration energy barrier. (d) Chronoamperometry (CA) tests for GCC and CPD-GCC cells. (e) EIS test for GCC//GCC and CPD-GCC//CPD-GCC cells. (f) Activation energy calculation. (g) The cycling curves and the current density of the half cell. (h) The voltage hysteresis at different current densities. (i) The calculated exchange current density.

number of lithium ions participate in charge transfer at the interface. This surpasses the charge transfer capacity of the lithium metal–electrolyte interface, leading to a potential difference between the anode and cathode in the symmetric cell, a phenomenon known as voltage hysteresis.

Therefore, the voltage hysteresis is primarily governed by the distribution of the ionic concentration field, the diffusion/transport rate of Li^+ ions, and the interfacial reaction kinetics. As demonstrated in Fig. 3d and e, the presence of lithiophilic functional groups on the CPDs leads to a more uniform Li^+ distribution and a smaller ionic concentration gradient on the CPD-GCC electrode surface. To further investigate the ion diffusion kinetics, we simulated the migration behavior of Li^+ ions on the surfaces of GCC and CPD-GCC electrodes (Fig. 5a and c). The Li^+ migration energy barrier on CPDs-GCC (0.22 eV) is significantly lower than that on GCC (0.35 eV), indicating that Li^+ ions migrate more easily on the CPD-GCC surface. As a result, at the same current density, the local ionic concentration on CPDs-GCC is lower than that on GCC. The chronoamperometry (CA) test further supports this conclusion, showing that Li^+ ions quickly enter a 3D diffusion regime on the CPD-GCC surface (Fig. 5d).

Additionally, symmetric cells were assembled using GCC//GCC and CPD-GCC//CPD-GCC configurations (without lithium deposition) to evaluate the ionic conductivity of the electrodes. As shown in Fig. 5e, the CPD-GCC electrode exhibits higher ionic conductivity than GCC. These findings collectively confirm that both on the electrode surface and within the bulk, Li^+ ions in CPDs-GCC can transport more rapidly, leading to a more uniform Li^+ concentration field.

Subsequently, we investigated the interfacial reaction kinetics. Electrochemical impedance spectroscopy (EIS) was conducted at various temperatures to calculate the activation energy for Li^+ interfacial charge transfer on both electrodes (Fig. S20†). As illustrated in Fig. 5f, the activation energy on CPDs-GCC is 17.37 kJ mol^{-1}, markedly lower than that on GCC (29.93 kJ mol^{-1}), indicating a faster interfacial reaction rate for Li^+ on CPDs-GCC. The time–voltage profiles of symmetric cells at different current densities were further evaluated. As the current density increased from 1 to 5 mA cm^{-2}, the voltage hysteresis increased accordingly. Compared with GCC, the CPD-GCC anode cell exhibits a lower voltage hysteresis, which can be attributed to the accelerated ion transport and interfacial reaction kinetics (Fig. 5g).

Additionally, we calculated the exchange current density (i_0) for both materials, as shown in the following equation:

$$i = i_0 \frac{2F}{RT}\eta$$

Here, i represents the current density, F is the Faraday constant, R is the gas constant, T is the temperature, and η denotes the voltage hysteresis of the battery (Fig. 5h). Linear

fitting analysis reveals that CPDs-GCC (i_0 = 3.211 mA cm^{-2}) exhibits a higher exchange current density compared to GCC (i_0 = 2.423 mA cm^{-2}) (Fig. 5i). This indicates that the lithiophilic functional groups of the CPDs accelerate the interfacial reaction kinetics of Li^+.

In summary, we believe that the introduction of lithiophilic functional groups on CPDs-GCC is the key factor enabling the electrode to exhibit an ultralow voltage hysteresis of 2 mV. Compared with GCC, Li^+ ions arriving at the electrode surface are rapidly dispersed due to the interaction with lithiophilic sites, which effectively reduces the local ion concentration. Meanwhile, at the electrode–electrolyte interface, Li^+ ions are quickly reduced and deposited, promptly consuming the accumulated Li^+ at the surface. This synergistic effect of enhanced surface diffusion and accelerated interfacial reaction results in ultralow voltage hysteresis maintained throughout long-term cycling.

2.5. Practical application of CPDs-GCC on full cells

Employing $LiFePO_4$ as the cathode, full cells were assembled to investigate the potential of the CPD-GCC anode in a practical battery system. Remarkably, the CPD-GCC//$LiFePO_4$ cell exhibits outstanding cycling stability with a capacity retention of 95% (139 mAh g^{-1}) after 3000 cycles, demonstrating the high Li utilization of the CPD-GCC anode (Fig. 6a). However, after 150 and 260 cycles, respectively, the specific capacity of CC and GCC full cells abruptly drops to a different degree. Fig. 6b shows the rate performances in detail. The cells of CPDs-GCC//$LiFePO_4$ demonstrate improved rate capability and greater discharge capacities of 141, 131, 117, 96 and 139 mA g^{-1}, respectively, at 0.5C, 1C, 2C, and 5C and return to 0.5C. Even at high rates of 2C and 5C, the capacity retention of the CPD-GCC cell is still higher than that of CC and GCC. Fig. 6c presents the voltage profiles of the CPD-GCC anode at the 0.5C, 1C, 2C, and 5C charging/discharging rates, illustrating its remarkable cycling ability. The cycling stability of CPDs-GCC exhibits a noteworthy level of competitiveness when compared to other 3D structure Li metal electrodes (Table S4†).

To further illustrate the practical utilization of the available flexibility of the CPD-GCC anode, a $LiFePO_4$ cathode/separator/CPD-GCC anode was employed for building a pouch cell. To seal the electrodes, two thin sheets of aluminum plastic film were employed, which had a surface area of roughly 3 × 3 cm^2. A flexible pouch cell (FPC) exhibits an initial voltage of 3.03 V, and it does not change even when bent, which demonstrates that the battery is both flexible and stable (Fig. 6d). The voltage of two FPCs in series is 5.97 V, demonstrating the feasibility of the method of connecting in series to provide higher voltages for electronic devices (Fig. S21†). Noticeably, a CPDs-

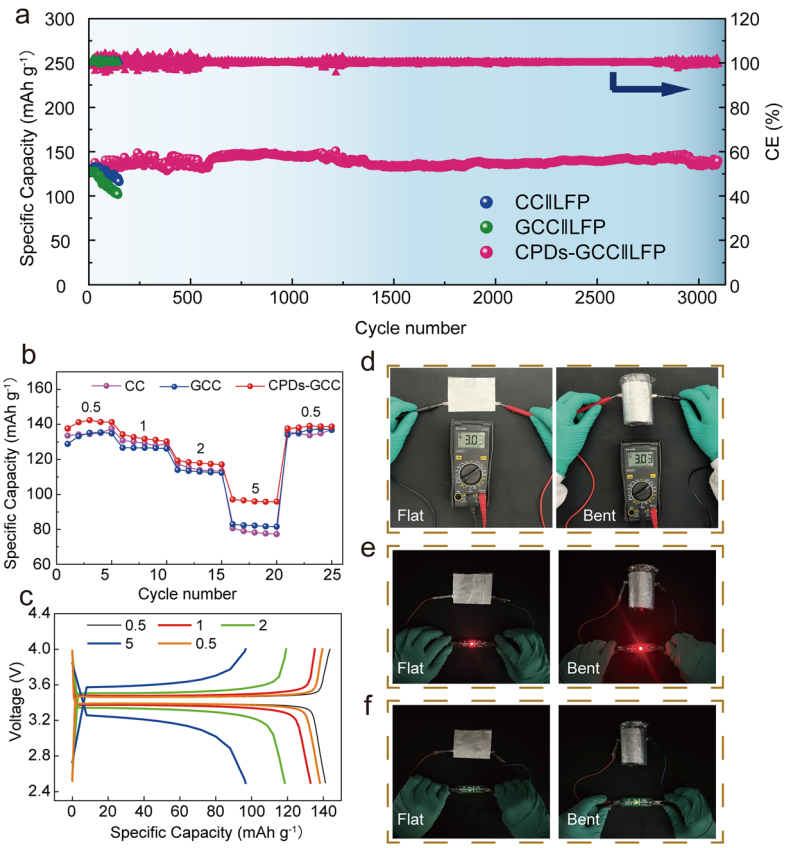

Fig. 6 (a) Cycling performances of the CPD-GCC//$LiFePO_4$ cell at 0.2 A g^{-1}. (b) Rate performances at different current densities. (c) Charging/discharging curves at different current densities of the CPD-GCC//$LiFePO_4$ battery. (d) The voltage of the CPD-GCC//$LiFePO_4$ flexible pouch cell in flat and bending states. (e and f) CPD-GCC//$LiFePO_4$ flexible pouch cell powering LEDs in flat and bending states.

GCC FPC powers two separate LEDs under both flat and bending conditions, indicating a possible application in flexible wearable electric devices (Fig. 6e and f).

3. Conclusions

In conclusion, we present a new approach for synthesizing a CPD composite carbon lithium 3D collector. The CPDs, rich in functional groups, promote uniform lithium metal growth on the anode and enhance ion transport and deposition kinetics, resulting in ultra-low voltage hysteresis. As a result, the assembled symmetric battery cycles stably for over 4800 hours with a voltage hysteresis as low as 2 mV. The full battery, paired with $LiFePO_4$, retains 95% of its capacity after 3000 cycles. This work explores the impact of voltage hysteresis on performance and introduces a simple method to reduce it, advancing the development of high-performance lithium metal batteries.

Author contributions

Jiayu Zhang: investigation, methodology, validation, and writing – original draft; Yanfei Li: conceptualization, methodology, and supervision; Yihan Song: methodology and validation; Guoduo Yang: data curation and project administration; Zhuo Wang: conceptualization and investigation; Xinyao Huang: conceptualization and formal analysis; Haizhu Sun: conceptualization, formal analysis, project administration, supervision, and writing – review and editing.

Conflicts of interest

There are no conflicts to declare.

Data availability

The data supporting this article have been included as part of the ESI.†

Acknowledgements

This work was supported by the National Natural Science Foundation of China (22275030, 22035001 and 22209023), Jilin Province Science and Technology Development Plan Project (International cooperation 20240402073GH).

References

1 H. Zhuang, H. Xiao, T. Zhang, F. Zhang, P. Han, M. Xu, W. Dai, J. Jiao, L. Jiang and Q. Gao, *Angew. Chem., Int. Ed.*, 2024, **63**, e202407315.
2 L. Liu, Z. Gong, C. Liu, A. Peng, Z. Zhang, J. Yu, J. Cai and Z. Yang, *Green Chem.*, 2024, **26**, 4168–4180.
3 H. Li, J. Wang, J. Zhang, L. Jia, H. Qu, Q. Guan, H. Zhang and H. Lin, *Green Chem.*, 2024, **26**, 10366–10382.
4 X. Chu, F. Dong, X. Zhang, Y. Liu, Y. Jiang and H. Xie, *J. Energy Storage*, 2024, **94**, 112447.
5 Y. Li, S. Ye, J. Lin, Y. Song, X. Wu, J. Zhang, C. Shao, Z. Su, H. Sun and D. S. Seferos, *Energy Environ. Mater.*, 2023, **6**, e12368.
6 G. Li, X. Duan, X. Liu, R. Zhan, X. Wang, J. Du, Z. Chen, Y. Li, Z. Cai, Y. Shen and Y. Sun, *Adv. Mater.*, 2023, **35**, 2207310.
7 Y. Li, Y. Hao, U. Ali, B. Liu, Q. Zhang, Z. Jin, L. Li, C. Wang and L. Zhang, *Inorg. Chem. Front.*, 2023, **10**, 5719.
8 W. Chen, S. Yu, Q. Sun, X. Shen, P. Shi, T. Yuan and Z. Lu, *Green Chem.*, 2025, **27**, 1696–1702.
9 D. Li, C. Xie, Y. Gao, H. Hu, L. Wang and Z. Zheng, *Adv. Energy Mater.*, 2022, **12**, 2200584.
10 W. Wang, Y. Song, G. Yang, R. Jiao, J. Zhang, X. Wu, J. Zhang, Y. Li, C. Tong and H. Sun, *Small*, 2023, **19**, 2206597.
11 P. Molaiyan, S. Bhattacharyya, G. S. dos Reis, R. Sliz, A. Paolella and U. Lassi, *Green Chem.*, 2024, **26**, 7508–7531.
12 J. Lv, B. Li, Q. Liu, Z. Gao, Z. Lang, S. Liang, Y. Li and H. Zang, *Angew. Chem., Int. Ed.*, 2023, **62**, e202306193.
13 G. Yang, B. Li, Y. Song, L. Ding, S. Gong, X. Wu, J. Zhang, Y. Li and H. Sun, *Electrochim. Acta*, 2022, **430**, 141035.
14 Z. Hao, Y. Lu, G. Yang, Q. Zhao, Z. Yan and J. Chen, *Adv. Mater.*, 2025, **37**, 2415258.
15 Y. Yu, X. Guo, Y. Liu, C. Liu, B. Liu, Q. Wang, Z. Sun, Y. Men, Y. Xie, Z. Xing and W. Hu, *Int. J. Biol. Macromol.*, 2025, **295**, 139560.
16 C. Fang, J. Li, M. Zhang, Y. Zhang, F. Yang, J. Z. Lee, M.-H. Lee, J. Alvarado, M. A. Schroeder, Y. Yang, B. Lu, N. Williams, M. Ceja, L. Yang, M. Cai, J. Gu, K. Xu, X. Wang and Y. S. Meng, *Nature*, 2019, **572**, 511–515.
17 P. Tan, Y. Wang, X. Sun, Y. Zhou, H. Dong, Y. Han and D. Li, *J. Alloys Compd.*, 2024, **996**, 174867.
18 A. M. Battaglia, E. Grignon, J. T. Liu and D. S. Seferos, *Small*, 2024, **20**, 2405118.
19 Z. Shi, Y. Wang, X. Yue, J. Zhao, M. Fang, J. Liu, Y. Chen, Y. Dong, X. Yan and Z. Liang, *Adv. Mater.*, 2024, **36**, 2401711.
20 H. Liu, J. Di, P. Wang, R. Gao, H. Tian, P. Ren, Q. Yuan, W. Huang, R. Liu, Q. Liu and M. Feng, *Carbon Energy*, 2022, **4**, 654–664.
21 J. Tan, L. Ma, P. Yi, Y. Wang, Z. Li, Z. Fang, X. Li, S. He, X. Wang, M. Ye and J. Shen, *Adv. Mater.*, 2024, **36**, 2403570.
22 Y. Jiang, X. Chu, J. Li, F. Dong, Q. Qiao, L. Cai, J. Liu and H. Xie, *J. Energy Storage*, 2025, **113**, 115686.
23 C. Xie, M. Rong, Q. Guo, Z. Wei, Z. Chen, Q. Huang and Z. Zheng, *Adv. Mater.*, 2024, **36**, 2406368.

24 W. Diao, D. Xie, Y. Wang, F. Tao, C. Liu, X. Wu, W. Li and J. Zhang, *Inorg. Chem. Front.*, 2024, **11**, 947–956.
25 Z. Kang, B. Yang and M. Prato, *Small*, 2023, **19**, 2304703.
26 S. Zhu, Q. Meng, L. Wang, J. Zhang, Y. Song, H. Jin, K. Zhang, H. Sun, H. Wang and B. Yang, *Angew. Chem., Int. Ed.*, 2013, **52**, 3953–3957.
27 Z. Chen, W. Chen, H. Wang, C. Zhang, X. Qi, L. Qie, F. Wu, L. Wang and F. Yu, *Nano Energy*, 2022, **93**, 106836.